3D printing of gaseous radiation detectors

F.M. Brunbauer,[a,b,1] **M. Lupberger,**[c] **H. Müller,**[a] **E. Oliveri,**[a] **D. Pfeiffer,**[b,a] **L. Ropelewski,**[a]
L. Scharenberg,[a,c] **P. Thuiner**[a] **and M. van Stenis**[a]

[a]*CERN,*
 385 Route de Meyrin 1217 Meyrin, Geneva, Switzerland

[b]*European Spallation Source (ESS AB),*
 P.O. Box 176, SE-22100 Lund, Sweden

[c]*University of Bonn,*
 Regina-Pacis-Weg 3, 53113 Bonn, Germany

 E-mail: florian.brunbauer@cern.ch

ABSTRACT: Additive manufacturing techniques such as 3D printing offer unprecedented flexibility in realising intricate geometries. Fused-filament fabrication and high-precision inkjet 3D printing of metals and polymers was used to create functional composite structures, which were operated as radiation detectors. Electron avalanche multiplication in a 3D printed structure was achieved. We present an ionisation chamber and a coarse 2D readout anode with orthogonal strips, which were printed with PLA and graphite-loaded PLA. High-resolution inkjet 3D printing was used to create a Thick Gaseous Electron Multiplier (THGEM). This represents the first realisation of a fully 3D printed structure achieving electron multiplication. Optical readout was used to quantify the gain factor of the structure and an image under X-ray irradiation was acquired. While the hole geometry of this prototype device inhibited high gain factors, it demonstrates that additive manufacturing is a viable approach for creating detector structures. The conventional manufacturing approach by photolithographic techniques will continue to dominate large size and volume production of MicroPattern Gaseous Detectors (MPGDs) but prototyping and results-driven detector optimisation may greatly benefit from the cost and time-effectiveness of 3D printing.

KEYWORDS: Detector design and construction technologies and materials; Gaseous detectors; Manufacturing; Micropattern gaseous detectors (MSGC, GEM, THGEM, RETHGEM, MHSP, MICROPIC, MICROMEGAS, InGrid, etc)

---

[1]Corresponding author.

Contents

1 Introduction

Radiation detector development has greatly benefited from advances in manufacturing techniques. The well-controlled photolithographic techniques from Printed Circuit Board (PCB) industry have led to the rise of MicroPattern Gaseous Detectors (MPGDs) and a multitude of detector geometries over the past decade. High-resolution photolithography and selective etching have been employed for MPGD varieties such as Gaseous Electron Multipliers (GEMs) [1] and MicroMesh Gaseous Structures (Micromegas) [2] and a mastery of these techniques has allowed for high-performance and large scale detection systems based on these technologies.

The rise of additive manufacturing techniques in industrial, research as well as consumer fields in recent years has led to a remarkable increase in the variety of applications in which 3D printing, selective laser sintering or stereolithography are used for. Ranging from low-cost 3D printers for personal use to biological material printing for medical applications [3] and metal printing, additive manufacturing technologies are able to fulfil distinguished requirements [4].

In the field of radiation detection, additive manufacturing has been used to print scintillating structures [5, 6]. For gaseous detectors, supporting mechanical components have previously been manufactured with 3D printing techniques. In a recent development, 3D printing was used to create a gas volume for a drift tube detector in which the amplifying element was a manually positioned stainless steel wire [7]. Until now, the active elements of detectors have been created with conventional approaches due to the limitations in feature size and material properties. Moreover, the requirement of printing polymer-metal composite structures to achieve functional components such as signal amplification stages has previously not been met by state-of-the-art technologies [8].

We report on the first application of Fused Filament Fabrication (FFF) and inkjet 3D printing techniques for manufacturing functional gaseous radiation detectors made of insulator-conductor composite structures. The focus on these two technologies comes from the fact that they do offer multi-material capabilities which are necessary for composite structures. The two technologies are schematically shown in figure 1.
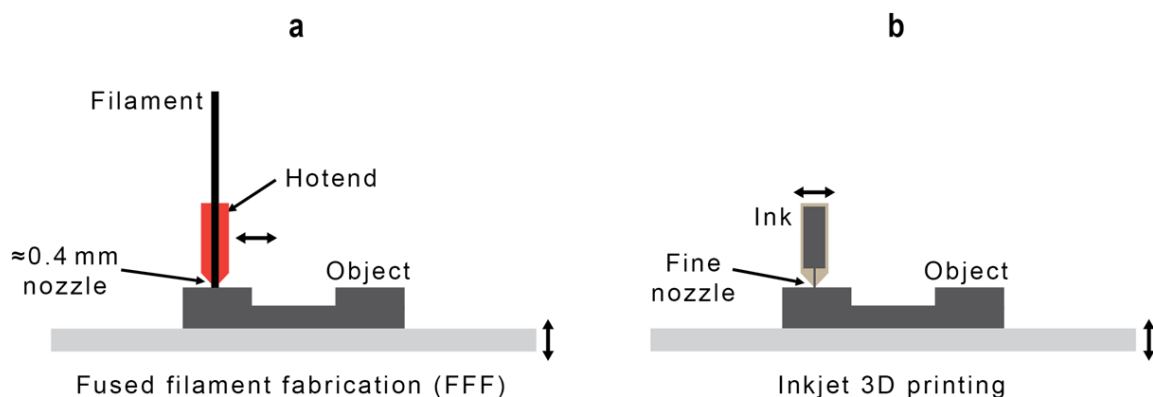
Figure 1. 3D printing technologies. (a) Fused filament fabrication (FFF). (b) Inkjet 3D printing. Schematics not drawn to scale.

FFF offers a low-cost entry point to the field of 3D printing and is the technology of choice for consumer-grade printers. It relies on extruding thermoplastics such as PoLyActide (PLA), Acrylonitrile Butadiene Styrene (ABS) or nylon through hot nozzles at temperatures around 200°C. Typical nozzles are around 400 μm in diameter which limits the achievable resolution to millimetre-scale structures. Many different models of FFF printers are commercially available including several with multiple nozzles, which may be used for multi-colour or multi-material prints. The requirement of low-melting temperatures limits the available filaments applicable for FFF but some engineered materials have been realised with properties ranging from haptic resemblance of other materials to magnetic or electrically conductive filaments. Low electric conductivity is achieved by graphite-loaded PLA filaments. While the volume resistivity of such materials is significantly higher compared to metals, values around 0.6 Ωcm [9] are sufficient for signalling or low-current applications.

To achieve high-resolution 3D printing, inkjet printing can be used. Based on print heads with hundreds of individual small nozzles, this approach resembles standard desktop inkjet printers with the exception of the materials used and the number of layers which are printed sequentially. This technology is pioneered by the company Nanodimension [10], which uses silver (Ag) colloid solutions and photopolymers as conductor and insulator materials, respectively. Micrometre-scale feature sizes are achieved by this technology and high electrical conductivity comparable to metals is provided by printed Ag structures. The technology is developed for PCB prototyping and capable of manufacturing multi-layer PCBs comparable to conventionally produced ones including RF compatibility and solderability [10].

2 Fused-filament fabrication

2.1 Ionisation chamber

An ionization chamber was printed by a commercial FFF 3D printer (Leapfrog Bolt [11]) with two print heads. While one head was used to print standard PLA for insulating structures such as the gas volume, the other one printed graphite-loaded conductive PLA to create two separate electrodes at a distance of 24 mm. Conductive PLA with a volume resistivity ranging from 30 Ωcm (across

layers) to 115 Ωcm (through layers) was used for the presented prints [12]. The CAD model of the ionization chamber is shown in figure 2a and the printed object in figure 2b.
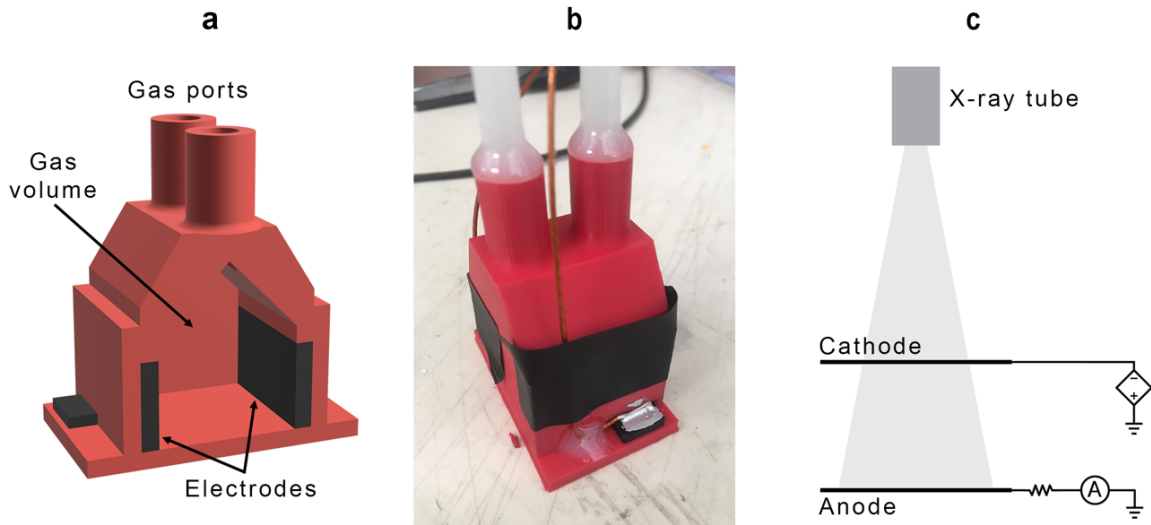

Figure 2. Ionisation chamber manufactured with FFF using insulating PLA (red) and graphite-loaded conductive PLA (black). (a) CAD model used for 3D printing. (b) Printed device connected to gas tubes and with high-voltage cables connected to the external electrodes. (c) Experimental setup used for characterisation of the response under X-ray irradiation. Schematic not drawn to scale.

The gas volume housing two electrodes featured two gas ports to which tubes were connected and sealed with adhesive. The small chamber was flushed with Ar/CO_2 (90/10%) at atmospheric pressure with a flow of 5 l/h. One of the electrodes was used as cathode and connected directly to a negative high-voltage supply. The other electrode was used as anode and connected to ground through a protection resistor and an ammeter used to measure the collected current as shown in figure 2c. The ionisation chamber was placed in front of a copper (Cu) target X-ray tube which was operated with an acceleration voltage of 20 kV and varying tube currents. The collected anode current was measured as a function of the X-ray tube current for different electric fields between the two electrodes ranging from 250 V/cm to 2000 V/cm as shown in figure 3.

While saturation attributed to recombination was observed for low electric fields, the response of the ionisation chamber was approximately linear over the full range of investigated irradiation intensities with an electric field of 2000 V/cm between the electrodes.

2.2 Readout strip anode

The same printing approach of combining PLA and graphite-loaded PLA with a dual-head FFF printer was also used to create a 2D strip anode with readout strips in orthogonal directions. The readout anode is shown in figure 4a. The bottom strips were 3 mm wide while the top strips were 2 mm wide. Bottom as well as top strips were located at a pitch of 6 mm and were 0.5 mm thick. The insulating layer between the strips was 0.5 mm thick. The electrical contact was brought to the back of the anode by printing a conductive path from the front to the back of the structure.

The readout anode was used to read out signals from a triple-GEM stack in a Time Projection Chamber (TPC) [13, 14] setup as shown in figure 4b. It was placed below the last GEM in the
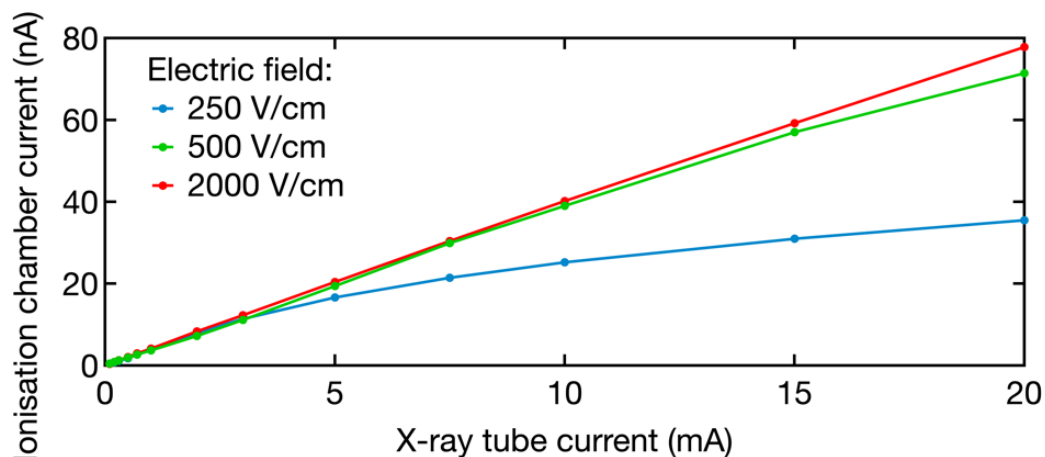
Figure 3. Anode current in 3D printed ionisation chamber as a function of X-ray tube current for different electric fields.
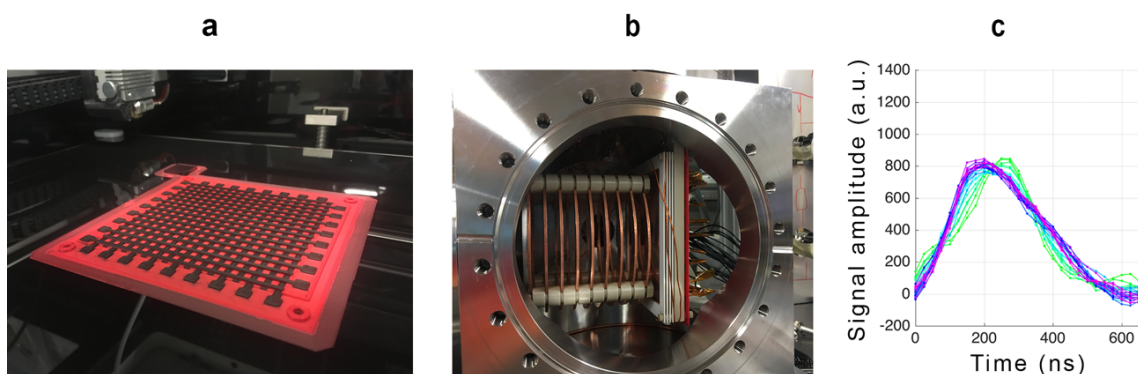

Figure 4. Readout strip anode with crossed strips in orthogonal directions. (a) 3D printed readout anode with an active area of $10\times10\,cm^2$. (b) TPC based on triple-GEM detector read out with 3D printed strip anode. (c) Signals of alpha particle event recorded from readout strips.

stack with an induction gap of 1 cm. The strips were connected to an APV25 ASIC [15] and read out by the RD51 Scalable Readout System (SRS) [16]. The APV25 was triggered by a signal from a PhotoMultiplier Tube (PMT) recording secondary scintillation light pulses. The detector was operated in an Ar/CF_4 (80/20%) gas mixture at atmospheric pressure at a flow rate of 5 l/h. A gaseous radon (Rn) source was used to bring alpha particles into the gaseous volume and individual events were recorded. Figure 4c shows an example of an alpha particle event with waveforms from different strips displayed. The shift in the arrival time of the pulses can be used to deduce the orientation and angle of the recorded alpha particle track.

Although it was possible to record electronic signals from a 3D printed composite readout strip anode, printing performant readout anodes remains challenging. The low conductivity of the graphite-loaded PLA might decrease the recorded signal amplitudes and modify the timing characteristics of electronic signals. Although higher conductivity filaments are available, the achieved conductivities are orders of magnitude below those of metals. Charging up effects might also affect the stability of recorded signals and remain to be investigated for 3D printed readout

structures. While these challenges might be addressed by future studies and optimisations, the resolution which can be achieved with FFF 3D printing limits the applicability of this manufacturing approach. With a nozzle size of approximately 0.4 mm, millimetre-scale structures can be achieved but strip widths below 0.5 mm and pitches below 1.5 mm are hard to achieve. This may be sufficient for some coarse applications but cannot be used to achieve fine readout structures for good spatial resolution. It is also not enough to 3D print amplifying structures capable of achieving electron avalanche multiplication.

3 Inkjet 3D printing

3.1 Thick Gaseous Electron Multiplier

High-resolution 3D printing with multiple materials was used to create a Thick Gaseous Electron Multiplier (THGEM) structure [17]. A THGEM geometry with a total active area of 5×5 cm^2 divided into two sectors with different hole diameters and pitches was designed. The CAD model featured cylindrical holes with diameters of 600 μm or 800 μm in the two sectors with a hole pitch of 1 mm or 1.5 mm, respectively. The nominal dielectric thickness was 400 μm and the nominal electrode thickness was 2 μm for both the top and bottom electrodes.

The employed 3D inkjet printing process is typically used for printing individual conductive traces on extended dielectric substrates for prototyping PCBs. The large conductor surfaces and relatively large thickness of the THGEM structure presented challenging conditions for the print process resulting in some adaptions of the printed geometry with respect to the CAD model. While these changes were not ideal for the operation of the THGEM structure, they might be improved by further process optimization.

Due to the printing process, the holes in the printed structure were conical instead of cylindrical and larger in diameter than desired. In the left sector of the THGEM shown in figure 5a, the hole diameter was increasing from 772 μm at the bottom to 928 μm at the top of the holes. In the right sector, the average hole diameters were increasing from 604 μm at the bottom to 790 μm at the top. The dielectric layer printed with polymer ink was 397 μm thick. The variation of the thickness of the printed structure across its surface was on the scale of micrometres. The thickness of electrodes printed with Ag nanoparticle ink was adjusted for low resistivity. While the bottom electrode was printed 2.8 μm thick, the top one was printed 21 μm thick as shown in figure 5c. The significantly larger thickness of the top electrode was necessary to achieve low resistance (<1 Ω between the two sides of the electrode) due to accumulated surface roughness during the printing process. The 3D inkjet printer deposits many layers consecutively to build up 3D structures from bottom to top and the resulting surface roughness of the dielectric layer required a thicker top electrode to ensure good electrical conductivity. The thickness variations of the structure can be seen in the microscopic image of the border between the two sectors in figure 5b.

Across each electrode, a resistance below 1 Ω was achieved. The top and bottom electrodes were separated by a resistance larger than 100 GΩ. The capacitance of each sector was approximately 110 pF. The device could withstand up to 1600 V potential difference in air. This is significantly lower compared to conventional THGEMs with a thickness of 400 μm, which can typically withstand well above 2000 V potential difference in air.
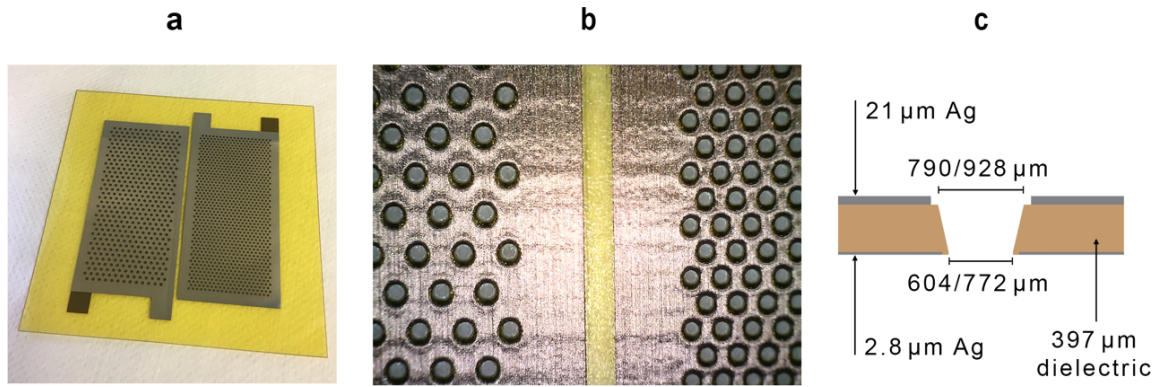
Figure 5. Printed THGEM detector. (a) Device with two sectors with different hole diameters and pitches. (b) Microscopic top view of the two sectors with different hole geometries along the border between them. (c) Measured dimensions of the THGEM structure. The two different numbers given for the top and bottom hole diameters correspond to the two sectors. Schematic not drawn to scale.

In contrast to the top electrode, the printed bottom electrode was very flat due to the fact that it was printed directly on the uniform print bed of the 3D inkjet printer. This difference in the visual appearance of the two electrodes can be seen in figure 6, where microscopic images of the top (a) and bottom (b) electrodes are shown.

Thin dielectric residuals were observed in the holes as shown in figure 6a, which are attributed to dielectric ink flowing down into the holes and accumulating on the print bed during the printing process before hardening. These residuals were effectively decreasing the free hole size in the printed THGEM. Manual removal of the residuals was possible, but they may be avoided in future prints by careful print parameter tuning.

As dielectric and conductive structures were printed consecutively with dedicated print heads, precise alignment between the two heads is important. Minor misalignment between the holes in the dielectric structure and in the printed electrodes was observed as shown in figure 6b. The magnitude of this misalignment varies across the active area of the device with almost perfect alignment achieved on one side and significant misalignment on the other side of the structure. This misalignment results in a crucial weakness in the high-voltage stability of the device. Due to the misalignment, the electrodes reach up to the hole in the dielectric without any rim remaining which is a weak point when high voltage is applied. Indeed, the regions with significant misalignment were found to be most susceptible to instabilities and discharges occurred predominantly where dielectric-conductor misalignment was most pronounced. Figure 6c shows a microscopic view of a region of the bottom electrode after discharges on several holes. Three holes with a strong discoloration around them are visible and the discharges appear to be focused on the side of the holes were the conductor reaches up the hole in the dielectric without any remaining rim. The maximum achievable voltage in an Ar/CO_2 (70/30%) gas mixture was limited to approximately 1100 V before discharges occurred frequently. Better alignment between dielectric and conductive structures may be achieved by further print process optimisations and might help to achieve significantly higher potential differences across the THGEM without the onset of discharges.

The THGEM was mounted in a gas volume to study its response as shown in figure 7a. To visualise signal amplification across the active area of the device, optical readout of the detector
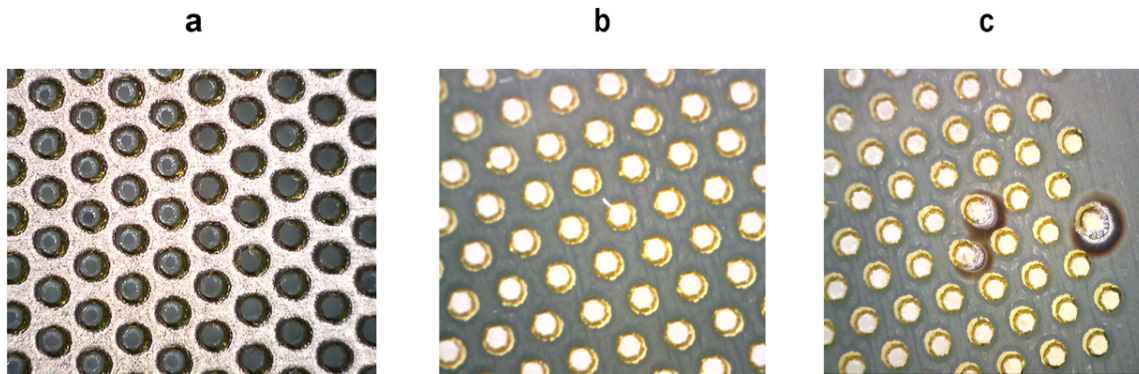
Figure 6. (a) Top electrode of THGEM. Dielectric residuals in the holes can be seen in the left four columns. These residuals were removed manually in the right four columns of holes. (b) Bottom electrode of the THGEM displaying misalignment of the holes in the dielectric and conductive structures. (c) Bottom electrode after several discharges in three holes.

under X-ray irradiation was used. The THGEM was placed between a thin foil cathode and a transparent ITO-based anode [18, 19]. The distances between the cathode and the THGEM as well as between the THGEM and the anode were 4 mm each. The gas volume was flushed with an Ar/CF$_4$ (80/20%) gas mixture at atmospheric pressure at a flow rate of 5 l/h. A gas mixture containing CF$_4$ was chosen for its high secondary scintillation light yield in the visible wavelength region [20] to allow for optical readout with CCD or CMOS cameras [21]. A low-noise CCD camera (QImaging Retiga R6 [22]) was placed outside of the gas volume at a distance of approximately 20 cm to record secondary scintillation light emitted during electron avalanche multiplication in the THGEM. The detector was irradiated with a Cu X-ray tube operated with an acceleration voltage of 20 kV and a tube current of 1 mA. The top electrode of the THGEM was biased with a negative high voltage power supply while the bottom electrode was grounded. A drift field of 50 V/cm and an induction field of 1000 V/cm were used. The potential difference across the THGEM was gradually increased up to 950 V where discharges started to occur. At each voltage, an image as shown in figure 7b was recorded with an exposure time of 10 s. A hardware binning setting of 8×8 pixels was used to collect signals of an 8×8 matrix of physical pixels and read them out as one virtual larger pixel, thus minimising the relative contribution of readout noise and increasing the signal-to-noise ratio while decreasing image resolution. Background images without X-ray irradiation were recorded and subtracted from the recorded images. The brightness of the resulting images was used as a quantification of the gain of the detector. Figure 7c shows the average pixel value intensity as a function of THGEM voltage where the onset of avalanche multiplication is visible around 300 V. Dividing the pixel value at the maximum THGEM voltage of 950 V by the one at low voltages, a gain factor of approximately 5 was determined. Instabilities of the detector at higher THGEM voltages prohibited higher gain factors.

To record spectra of the electronic signals from the THGEM detector, it was mounted as the first amplification stage in a triple-stage detector above two conventional GEM foils as shown in figure 8a. Signals were recorded from a pad anode with amplifying and signal shaping electronics and a Multi-Channel Analyser (MCA) to acquire histograms of signal amplitudes. In this setup, the detector was operated in an Ar/CO$_2$ (70/30%) gas mixture at atmospheric pressure at a flow rate of
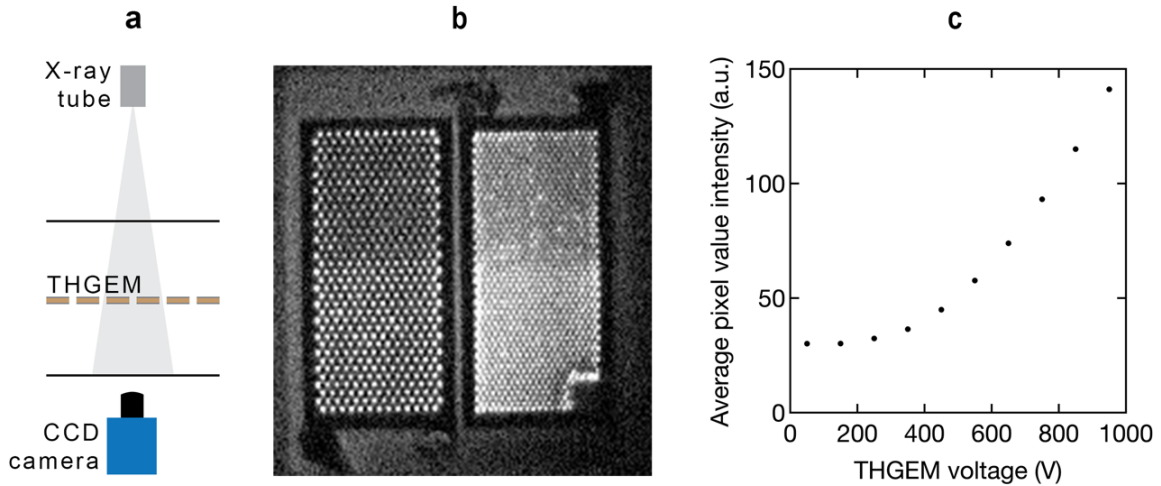
Figure 7. Optical readout of printed THGEM. (a) X-ray irradiation setup with THGEM and optical readout. Schematic not drawn to scale. (b) Optically read out image with a THGEM voltage of 950 V. The bottom right corner was disconnected after destructive discharges. The dielectric residuals in the holes shown in figure 6a were removed from the top halves of both sectors. The higher pixel values observed in the bottom halves of the sectors are attributed to the confinement of the holes by the remaining dielectric residuals in these regions. (c) Pixel value intensity as a function of THGEM voltage.

5 l/h. The THGEM was placed 4 mm below the cathode and 3 mm above the first of the two GEM foils. A transfer gap of 2 mm was used between the two GEM foils. The anode was placed 3 mm below the last GEM foil. In the drift region, an electric field of 50 V/cm was applied. In the transfer region between the THGEM and the GEM foil, a transfer field of 1500 V/cm was used. An induction field of 2000 V/cm between the last GEM foil and the anode was used. The two GEM foils were operated with a voltage difference of 430 V across each GEM. The detector was irradiated with a collimated ^{55}Fe source. The charging up behaviour of the THGEM structure was not addressed in this study and will need to be investigated to understand the dynamics of the detector response under irradiation. The ^{55}Fe source used to record energy spectra had a considerably lower rate than the X-ray tube used to record optically read out images as shown in figure 7. Thus, the time scales of charging up of the THGEM detector may be significantly different.

The acquired energy spectra from the detector for different THGEM voltages are shown in figure 8b. The peak at an amplitude around 250 is the signal from X-ray photons converting between the THGEM and the GEM foils. Events converted in this region are amplified only by the two GEM foils and their amplitude is independent of the THGEM voltage. Thus, this peak remains at the same amplitude for all THGEM voltages. The dominant peak at lower amplitudes is composed of X-rays interacting in the drift region between the cathode and the THGEM and its position thus depends on the THGEM voltage. For higher THGEM voltages, the peak is shifted to higher amplitudes. Since the gain of the two GEM foils was kept constant, this shift reflects signal amplification in the THGEM. The significant width of the spectra and their degradation with higher THGEM voltages is attributed to poor collection and extraction of electrons from the holes of the THGEM due to geometrical issues as shown in figure 6. In the case of optical readout, scintillation light produced in the holes can be recorded independently of electron extraction from the holes and this effect was therefore not observed in the measurement shown in figure 7c.
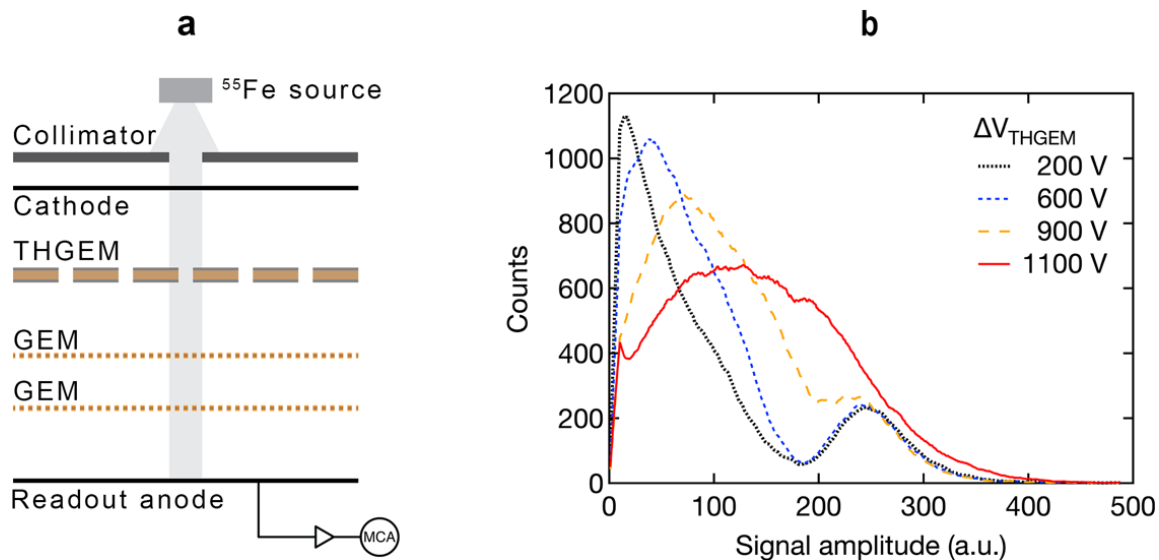
– 8 –

Figure 8. Electronic readout of printed THGEM. (a) X-ray irradiation setup with THGEM placed in a gas volume above two standard GEM foils. Signals from the anode were recorded with a Multi-Channel Analyser (MCA). Schematic not drawn to scale. (b) Histogram of anode signal amplitudes for different THGEM voltages.

The discrepancy between the optical and electronic measurements is attributed to the poor electron transfer through the THGEM. This inhibits the recording of energy spectra resolving the double peak structure of ^{55}Fe in gaseous detectors and the quantification of the gain of this structure from electronic signals and will be addressed in further studies. Nevertheless, signal amplification can be observed in the recorded energy spectra and improved print quality may increase the collection and extraction efficiencies of the device.

4   Conclusion

Additive manufacturing can be used to create functional gaseous radiation detectors. Multi-material FFF 3D printing was employed to manufacture an ionisation chamber which displayed a linear response to X-ray radiation. In addition, a 2D strip anode was printed and used to read out electronic signals from a triple-GEM detector. FFF 3D printing may be used for coarse geometries including pad readout anodes with varying pad sizes as well as intricate 3D structures. However, it does not allow for sufficient resolution to create amplifying structures.

Multi-material inkjet 3D printing enables high-resolution functional structures and was used to print a THGEM structure. The THGEM was operated in Ar/CO$_2$ and Ar/CF$_4$ gas mixtures and read out by optical and electronic means. Signal amplification in the 3D printed structure could be observed. Process related issues such as misalignment of dielectric and conductive materials and dielectric residues in the holes limited the maximum voltage and thus the achievable gain in the device and are subject to further process optimisation.

Additive manufacturing may enable advanced detector geometries not accessible by photolithographic techniques and allow for MPGD structures which are inherently stable against discharges.

Precise multi-material 3D printing of functional devices could significantly benefit radiation detector research by offering a fast and cost-effective approach to prototyping and can enable results-driven detector optimisation.

Acknowledgments

References

[1] F. Sauli, *GEM: A new concept for electron amplification in gas detectors*, *Nucl. Instrum. Meth.* **A 386** (1997) 531.

[2] Y. Giomataris, P. Rebourgeard, J.P. Robert and G. Charpak, *MicrOMEGAs: A high granularity position sensitive gaseous detector for high particle flux environments*, *Nucl. Instrum. Meth.* **A 376** (1996) 29.

[3] H.N. Chia and B.M. Wu, *Recent advances in 3D printing of biomaterials*, *J. Biol. Eng.* **9** (2015) 1.

[4] K.V. Wong and A. Hernandez, *A Review of Additive Manufacturing*, *ISRN Mech. Eng.* **2012** (2012) 1.

[5] Y. Mishnayot, M. Layani, I. Cooperstein, S. Magdassi and G. Ron, *Three-dimensional printing of scintillating materials*, *Rev. Sci. Instrum.* **85** (2014) 085102 [`arXiv:1406.4817`].

[6] J. Son et al., *Improved 3D Printing Plastic Scintillator Fabrication*, *J. Korean Phys. Soc.* **73** (2018) 887.

[7] S. Fargher, C. Steer and L. Thompson, *The Use of 3D Printing in the Development of Gaseous Radiation Detectors*, *EPJ Web Conf.* **170** (2018) 01016.

[8] M. Hohlmann, *Printing out Particle Detectors with 3D-Printers, a Potentially Transformational Advance for HEP Instrumentation*, in *Proceedings, 2013 Community Summer Study on the Future of U.S. Particle Physics: Snowmass on the Mississippi (CSS2013): Minneapolis, MN, U.S.A., July 29 – August 6, 2013*, `arXiv:1309.0842`.

[9] Black Magic 3D, *Black Magic 3D*, https://www.blackmagic3d.com, (8 May 2018).

[10] *Nano Dimension*, www.nano-di.com, (20 September 2019).

[11] Leapfrog 3D Printers, *Leapfrog 3D Printer s*, https://www.lpfrg.com, (7 May 2018).

[12] Protoplant, *Proto-pasta*, www.proto-pasta.com, (30 September 2019).

[13] D.R. Nygren, *The Time Projection Chamber — A New 4pi Detector for Charged Particles*, eConf **C740805** (1974) 58.

[14] F.M. Brunbauer et al., *Live event reconstruction in an optically read out GEM-based TPC*, *Nucl. Instrum. Meth.* **A 886** (2018) 24.

[15] M.J. French et al., *Design and results from the APV25, a deep sub-micron CMOS front-end chip for the CMS tracker*, *Nucl. Instrum. Meth.* **A 466** (2001) 359.

[16] S. Martoiu, H. Müller, A. Tarazona and J. Toledo, *Development of the scalable readout system for micro-pattern gas detectors and other applications*, 2013 *JINST* **8** C03015.

[17] R. Chechik, A. Breskin, C. Shalem and D. Mörmann, *Thick GEM-like hole multipliers: Properties and possible applications*, *Nucl. Instrum. Meth.* **A 535** (2004) 303 [`physics/0404119`].

[18] T. Fujiwara, Y. Mitsuya, T. Yanagida, T. Saito, H. Toyokawa and H. Takahashi, *High-photon-yield scintillation detector with Ar/CF 4 and glass gas electron multiplier*, *Jap. J. Appl. Phys.* **55** (2016) 106401.

[19] F.M. Brunbauer et al., *Combined Optical and Electronic Readout For Event Reconstruction in a GEM-based TPC*, *IEEE Trans. Nucl. Sci.* **65** (2018) 913.

[20] M.M.F.R. Fraga, F.A.F. Fraga, S.T.G. Fetal, L.M.S. Margato, R. Ferreira-Marques and A.J. P.L. Policarpo, *The GEM scintillation in He CF-4, Ar CF-4, Ar TEA and Xe TEA mixtures*, *Nucl. Instrum. Meth.* **A 504** (2003) 88.

[21] F.M. Brunbauer et al., *Radiation imaging with optically read out GEM-based detectors*, 2018 *JINST* **13** T02006.

[22] QImaging Corporation, *Retiga R6*, (2016).